

Study of the convergence of the Meshless Lattice Boltzmann Method in Taylor-Green and annular channel flows

Dawid Strzelczyk^{1,*} and Maciej Matyka¹

¹Institute of Theoretical Physics,
Faculty of Physics and Astronomy,
University of Wrocław,
pl. M. Borna 9, 50-204, Wrocław, Poland

*dawid.strzelczyk@uwr.edu.pl

ABSTRACT

The Meshless Lattice Boltzmann Method (MLBM) is a numerical tool that relieves the standard Lattice Boltzmann Method (LBM) from regular lattices and, at the same time, decouples space and velocity discretizations. In this study, we investigate the numerical convergence of MLBM in two benchmark tests: the Taylor-Green vortex and annular (bent) channel flow. We compare our MLBM results to LBM and to the analytical solution of the Navier-Stokes equation. We investigate the method's convergence in terms of the discretization parameter, the interpolation order, and the LBM streaming distance refinement. We observe that MLBM outperforms LBM in terms of the error value for the same number of nodes discretizing the domain. We find that LBM errors at a given streaming distance δx and timestep length δt are the asymptotic lower bounds of MLBM errors with the same streaming distance and timestep length. Finally, we suggest an expression for the MLBM error that consists of the LBM error and other terms related to the semi-Lagrangian nature of the discussed method itself.

Keywords: Lattice Boltzmann Method, meshless methods, radial basis functions, convergence analysis

1 Introduction

A challenging task preceding most computational fluid dynamics calculations is discretizing the domain. It often consists of complex geometries, especially in flows through porous media¹, biological structures², past cars³ and marine vehicles⁴ which makes the use of irregular discretizations inevitable. In such cases, standard approaches, such as the Finite Volume Method, need to perform intensive computations at the level of domain discretization, not only to place nodes in the domain but also to connect them in such a way that they tessellate the space properly⁵. Thus, additional memory is required to store information about the connectivity between nodes. Moreover, local, adaptive refinement of the discretization, which aims to increase the solution accuracy only where necessary, implies costly mesh manipulations even during the simulation runtime. A remedy for these issues is to use meshless methods in which domains are discretized with clouds of non-connected points⁶. They allow for more freedom in the node placement in the domain, a less costly local refinement procedure due to the lack of node connectivity information, and feasible formulation of high-order approximations. However, this comes at the cost of, for example, conservation laws not being imposed explicitly on the solved equations. One of the meshless methods is the radial basis functions (RBF) method⁷⁻⁹ where interpolation and derivatives approximation are performed in radial functions basis.

One does not need to solve the Navier-Stokes equation directly to obtain quantities such as fluid velocity and pressure. The desired quantities can be calculated by solving Boltzmann's transport equation (BTE). Lattice Boltzmann Method (LBM)¹⁰ is a numerical tool for solving BTE that has in the last decades become a popular method of choice for simulating transport phenomena. It is advantageous compared to the direct Navier-Stokes solution methods in terms of stability, ease of parallelization, and simplicity of implementation. Applications range from porous media flows^{1,11,12}, multiphase flows^{13,14} including cavitating flows¹⁵ to the flow of semiclassical fluids¹⁶ and relativistic hydrodynamics¹⁷. In its standard formulation, the LBM operates on regular square (in 2D) discretization (lattices) of the space, which is related to the discretization of particle velocities. There are numerous works where the standard algorithm is extended to use unstructured discretizations to allow for a better representation of the underlying geometry in the model and provides more freedom for the placement of the nodes inside the domain. For example in¹⁸ a cylindrical mesh with second order interpolation is used to simulate flow around a cylinder, whereas in¹⁹ rectangular meshes of various densities along with linear and quadratic interpolation are used to model the flow in

a channel behind a sudden contraction. A method that utilizes Lagrange polynomials of various orders in periodic flows was investigated in²⁰. The approaches put forward in²¹ and²² use finite elements to solve the weak forms of the discrete Boltzmann equation. A more general discussion on solving BTE with finite elements on unstructured discretizations is presented in²³.

The authors of²⁴ develop an MLBM algorithm capable of operating on clouds of scattered, non-connected points instead of grids. This method uses radial basis function interpolation to solve the streaming step in a semi-Lagrangian way. Although the original method seems promising and proves the numerical accuracy of the obtained results of the flow, its convergence toward the analytical solution was neither tested nor discussed. Thus, in this work, we aim to address the question of the spatial convergence of MLBM presented in²⁴. In contrast to the original work, where regular or O-type grids were used, we perform a systematic study using node sets more suited for meshless methods. For the benchmark, we choose two distinct flows: the Taylor-Green vortex and a flow in an annular channel. For both, we use irregular spatial discretizations generated by the algorithm from²⁵ based on Poisson disk sampling. Our results show, that although LBM errors are in principle smaller, there are regions in which MLBM outperforms it and may be a good alternative, especially in systems with irregular boundaries.

2 Methods

2.1 Lattice Boltzmann Method

Lattice Boltzmann Method^{10,26} solves equations governing the evolution of discrete velocities distribution function:

$$f_k(t+1, x) = f_k^{\text{post}}(t, x + e_{k'}) \quad (1)$$

where f_k is the distribution function associated with the k -th streaming vector e_k , k' denotes the direction opposite to k ($e_k = -e_{k'}$) and the superscript 'post' denotes the post-collision distribution function. According to this notation, $x + e_{k'}$ denotes the neighbor of lattice node x lying one lattice site in the upstream direction e_k from this node. Note that Eq. (1) is written in non-dimensionalized form with the timestep length equal to 1. We use D2Q9 BGK model with 9 streaming directions ($k = 0, 1, \dots, 8$):

$$e_k \in ((0, 0), (1, 0), (0, 1), (-1, 0), (0, -1), (1, 1), (-1, 1), (-1, -1), (1, -1)) \quad (2)$$

which imposes the use of a square lattice. Refer to Fig. 1 for a graphical representation of the LBM lattice and streaming directions. The mentioned model uses f_k^{post} in the form suggested by Bhatnagar, Gross and Krook (BGK)²⁷:

$$f_k^{\text{post}} = f_k(t, x) - \frac{1}{\tau} [f_k(t, x) - f_k^{\text{eq}}(t, x)] \quad (3)$$

where τ , the so-called *relaxation time*, determines the characteristic timescale of the particle populations reaching local equilibrium. The equilibrium distributions f_k^{eq} are expressed as:

$$f_k^{\text{eq}}(t, x) = \omega_k \rho \left[1 + \frac{c_k \cdot u}{c_s^2} + \frac{(c_k \cdot u)^2}{2c_s^4} - \frac{u^2}{2c_s^2} \right] \quad (4)$$

where $c_s = 1/\sqrt{3}$ denotes the lattice speed of sound. ω_k is the weight specific to the k th streaming direction:

$$\omega = \left(\frac{4}{9}, \frac{1}{9}, \frac{1}{9}, \frac{1}{9}, \frac{1}{9}, \frac{1}{36}, \frac{1}{36}, \frac{1}{36}, \frac{1}{36} \right). \quad (5)$$

The nondimensionalized kinematic viscosity of the modeled fluid can be calculated as $\nu_{lb} = (\tau - 0.5)/c_s^2$. Macroscopic density and velocity, $\rho = \rho(t, x)$ and $u = u(t, x)$ respectively, at time t and point x , are obtained from discrete populations:

$$\rho = \sum_{k=1}^q f_k \quad (6)$$

$$u = \frac{1}{\rho} \sum_{k=1}^q f_k e_k$$

In the numerical implementations, at each time step, Eq. (3) is first calculated to obtain the values of the post-collision distribution function (*collision step*). Then, (1) advects post-collision distributions to neighboring nodes (*streaming step*). Because lattice nodes x coincide with the departure/arrival nodes of the streaming step, transport is purely Lagrangian and amounts to an index shift in the distribution function array.

2.2 Radial Basis Functions interpolation

We use meshless interpolation in radial functions basis to perform the semi-Lagrangian streaming step of the LBM. Consider a set of N points in d -dimensional Euclidean space $x_i \in \mathbb{R}^d$, $i = 1, 2, \dots, N$ forming a set $X = \{x_1, x_2, \dots, x_N\}$. Each point can be assigned a set $X^L \subset X$, $L = 1, \dots, N$ of its closest neighbors, including the node itself. We denote N_L members of X^L as x_i^L , $i = 1, \dots, N_L$. We assume that in every set X^L the first node $x_1^L \equiv x_i$ and we call this node the *stencil center*. We also assume that, at every point $x \in X$ we know the value $f_i \equiv f(x_i)$ of the interpolated function f . In our case, these are the nine distribution functions introduced in the previous section. In each of X^L sets one can construct local RBF interpolants F_L :

$$F_L(x) = \sum_{i=1}^{N_L} \gamma_i^L \phi_i^L(x) + \sum_{j=1}^{N_L^p} \pi_j^L p_j^L(x) \approx f(x) \quad (7)$$

where $\phi_i^L(x) \equiv \phi_i(|x - x_i^L|) \equiv \phi_i(r)$ and $p_j^L(x)$ are radial functions and polynomials forming the RBF and polynomial subsets of the interpolation basis, respectively. γ_i^L and π_j^L are coefficients of the linear combination of the interpolation basis elements. It can be written in vector form as:

$$F_L(x) = [\gamma_L^T, \pi_L^T] \cdot \phi_L \approx f(x) \quad (8)$$

where coefficient vectors γ_L and π_L are given as:

$$\gamma_L = \begin{Bmatrix} \gamma_1^L \\ \gamma_2^L \\ \vdots \\ \gamma_{N_L}^L \end{Bmatrix}, \quad \pi_L = \begin{Bmatrix} \pi_1^L \\ \pi_2^L \\ \vdots \\ \pi_{N_L^p}^L \end{Bmatrix} \quad (9)$$

and ϕ_L is the vector of X^L 's basis functions values at point x :

$$\phi_L(x) = [\phi_1^L(x), \dots, \phi_{N_L}^L(x), p_1^L(x), \dots, p_{N_L^p}^L(x)]^T \quad (10)$$

Vectors γ_L and π_L are determined in each set X^L by the following set of *collocation equations*:

$$\Phi_L \cdot \begin{Bmatrix} \gamma_L \\ \pi_L \end{Bmatrix} = \begin{bmatrix} R_L & P_L \\ P_L^T & 0 \end{bmatrix} \cdot \begin{Bmatrix} \gamma_L \\ \pi_L \end{Bmatrix} = \begin{Bmatrix} f_L \\ 0 \end{Bmatrix} \quad (11)$$

where 0 is either a $N_L^p \times N_L^p$ matrix of zeros or N_L^p -element vector of zeros and f_L is an array of the interpolated function values at X^L members:

$$f_L = [f(x_1^L), \dots, f(x_{N_L}^L)]^T. \quad (12)$$

The RBF interpolation matrix R_L and the polynomial interpolation matrix P_L are given as

$$R_L = \begin{bmatrix} \phi_1^L(x_1^L) & \phi_2^L(x_1^L) & \cdots & \phi_{N_L}^L(x_1^L) \\ \phi_1^L(x_2^L) & \phi_2^L(x_2^L) & \cdots & \phi_{N_L}^L(x_2^L) \\ \vdots & \vdots & \ddots & \vdots \\ \phi_1^L(x_{N_L}^L) & \phi_2^L(x_{N_L}^L) & \cdots & \phi_{N_L}^L(x_{N_L}^L) \end{bmatrix} \quad (13)$$

$$P_L = \begin{bmatrix} p_1^L(x_1^L) & p_2^L(x_1^L) & \cdots & p_{N_L^p}^L(x_1^L) \\ p_1^L(x_2^L) & p_2^L(x_2^L) & \cdots & p_{N_L^p}^L(x_2^L) \\ \vdots & \vdots & \ddots & \vdots \\ p_1^L(x_{N_L}^L) & p_2^L(x_{N_L}^L) & \cdots & p_{N_L^p}^L(x_{N_L}^L) \end{bmatrix}$$

Transforming Eq. (11), the coefficient vectors can be written as:

$$\begin{Bmatrix} \gamma_L \\ \pi_L \end{Bmatrix} = \Phi^{-1} \cdot \begin{Bmatrix} f_L \\ 0 \end{Bmatrix} \quad (14)$$

with the use of which one can rewrite Eq. (8) as:

$$F_L(x) = \left(\Phi^{-1} \cdot \begin{Bmatrix} f_L \\ 0 \end{Bmatrix} \right) \cdot \phi_L(x) \approx f(x) \quad (15)$$

and by rearranging terms:

$$F_L(x) = (\Phi^{-1} \cdot \phi_L(x)) \cdot \begin{Bmatrix} f_L \\ 0 \end{Bmatrix} = w_L(x) \cdot \begin{Bmatrix} f_L \\ 0 \end{Bmatrix} \approx f(x) \quad (16)$$

In this manner, one defines the value of interpolant F_L at an arbitrary point x in terms of the interpolated function values f_L and the *shape vector* $w_L(x)$.

2.3 Meshless LBM with RBF interpolation

We use the D2Q9 BGK LBM model and solve the streaming step in a semi-Lagrangian way using RBF interpolation. Because departure nodes ($x + e_k$ in Eq. (1)) need no longer to coincide with the lattice points we find it more convenient to introduce streaming length δx_{ML} and timestep length δt , both in physical units, to describe the model. In this manner lattice directions e_k are substituted with *lattice velocities* $c_k = e_k \delta x_{ML} / \delta t$. To relate meshless and standard LBM setups to one another, one can introduce the standard LBM discretization parameter $\delta x = L_0 / N_L$ where L_0 is some physical reference length and N_L is the number of lattice nodes discretizing it and compare δx_{ML} with δx . It is also necessary to distinguish between *Eulerian nodes*, where the values of distribution functions are stored and where collisions take place, and *Lagrangian nodes*, which serve only as departure nodes for distribution functions during streaming (see the right subplot of Fig. 1).

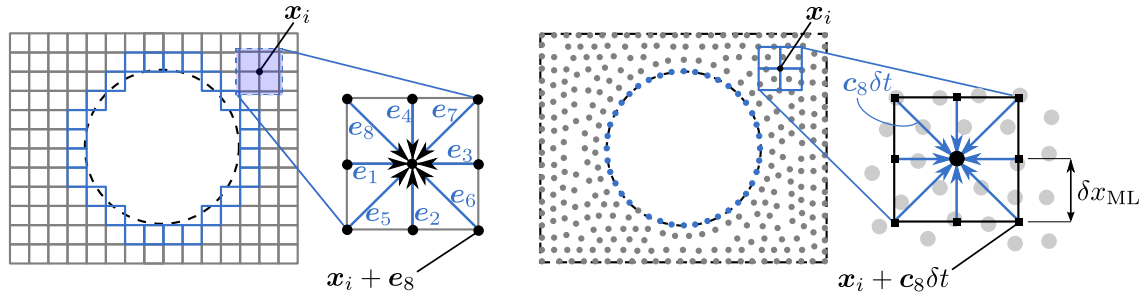


Figure 1. *Left:* a regular LBM grid discretizing a circle (dashed line) with a zoom at a local neighborhood of a discretization node. Note that the boundary is discretized in a stair-shaped manner (blue squares). *Right:* a meshless discretization of the same geometry results in nodes lying exactly on the boundary. Local neighborhoods are built for each node similar to the lattice approach but with the streaming directions e_k replaced by streaming velocities c_k .

In the semi-Lagrangian approach, the collision step is performed, due to its local nature, in the same way as in the standard LBM - in each Eulerian point. Streaming step, solved in a semi-Lagrangian way consists of interpolating the values of distribution functions from Eulerian to Lagrangian nodes and then advecting the interpolated distributions to the target Eulerian nodes. Refer to Figure 2 for a graphical interpretation of the above three steps. Giving up the Lagrangian nature of the streaming step decouples velocity and space discretizations since Lagrangian nodes positions $x + c_k \delta t = x + \delta x_{k'}$ need not to coincide with any of Eulerian nodes.

To perform interpolation we find the closest Eulerian neighbor of each Lagrangian point and determine the members of its stencil. Then, the interpolation of the distribution functions to each Lagrangian point is performed within this stencil. We use stencils of size $N_L = 25$. Interpolation basis consists of cubic RBFs ($\phi(r) = r^3$) augmented with two-dimensional polynomial sets \mathcal{P}_i^2 of orders $i = 2, 4$:

$$\begin{aligned} \mathcal{P}_2^2 &= \{1, x, y, x^2, xy, y^2\} \\ \mathcal{P}_4^2 &= \mathcal{P}_2^2 \cup \{x^3, x^2y, xy^2, y^3, x^4, x^3y, x^2y^2, xy^3, y^4\}. \end{aligned} \quad (17)$$

The size of the polynomial subset of the interpolation basis introduced in Eq. (7) is equal to the power of \mathcal{P}_i^2 : $N_L^p = |\mathcal{P}_i^2|$. Inverting local interpolation matrices Φ_L is performed using LU decomposition^{28,29} with partial pivoting implemented in the `PartialPivLU` solver of the Eigen library³⁰. The complete algorithm of the meshless LBM is presented in Appendix A.

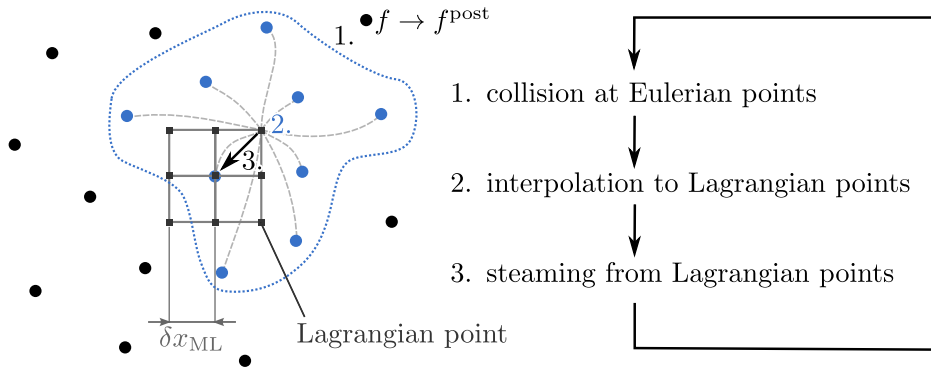


Figure 2. The procedure performed at a single timestep of the meshless LBM algorithm. Circles represent Eulerian points, squares denote Lagrangian points. A dashed loop encloses the stencil of a Lagrangian node which consists of the 9 closest neighbors of the Lagrangian node (blue circles). The interpolated distribution function is streamed to the Eulerian point lying at the center of the presented square lattice.

3 Results

We consider the Taylor-Green vortex flow as a benchmark test³¹. It is a popular flow problem devoid of walls and is thus suitable for the study of the convergence of numerical methods with no errors introduced by factors other than periodic boundary conditions. The domain is a two-dimensional square $D = [0, 1] \times [0, 1]$ with periodic boundary conditions. The velocity field of the flow is given by:

$$\begin{aligned} u_{true}(t, x, y) &= U_0 \cos 2\pi x \sin 2\pi y e^{(-2\nu k^2 t)} \\ v_{true}(t, x, y) &= -U_0 \sin 2\pi x \cos 2\pi y e^{(-2\nu k^2 t)}, \quad t \geq 0 \end{aligned} \quad (18)$$

with scaling parameter $k = 2\pi L$ dependent on the domain side length $L = 1$, the velocity magnitude $U_0 = 1$ and kinematic viscosity $\nu = 1$.

In the meshless formulation, periodicity is implemented through a periodic search of the closest Eulerian neighbors and interpolation stencil members. The domain is discretized with an irregular point cloud obtained from the algorithm²⁵ based on Poisson disk sampling implemented in the Medusa library³². After nodes generation, we run several relaxing iterations so that the nodes are distributed more uniformly, particularly to eliminate artifacts introduced by domain corners. Fig. 3 shows the point clouds used in the calculations.

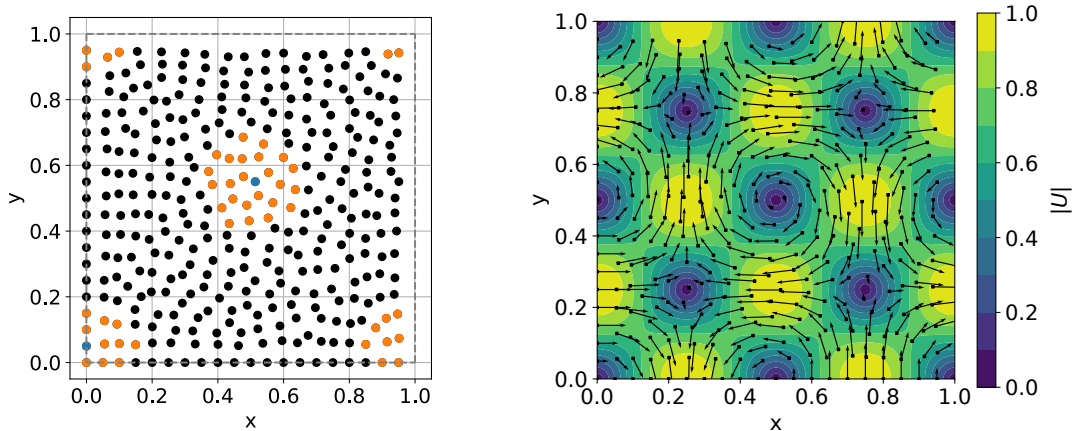


Figure 3. *Left:* the $h = 1/20$ meshless domain used in Taylor-Green vortices test. A dashedline denotes the periodic boundary. Orange points are the members of the stencils of the two blue points. *Right:* a velocity map and vectors of the initial condition of the Taylor-Green vortex. For a clearer visualization of vectors a coarser discretization was used here compared to the left plot.

We use two measures of discretization refinement for the meshless LBM. The first is the square root of the number of Eulerian nodes in the domain, which is inversely proportional to the average distance between Eulerian nodes, $\sqrt{N} \sim h^{-1}$. This

directly affects the interpolation accuracy. The other is the streaming distance δx_{ML} , which determines the LBM-related errors of the meshless formulation (see Fig. 4). In the standard LBM, the solution error depends only on the square root of the number of nodes in the domain \sqrt{N} . At the same time, \sqrt{N} is a measure of computational and memory demands of each method and will be used as the main parameter for the comparison between them during the discussion on accuracy.

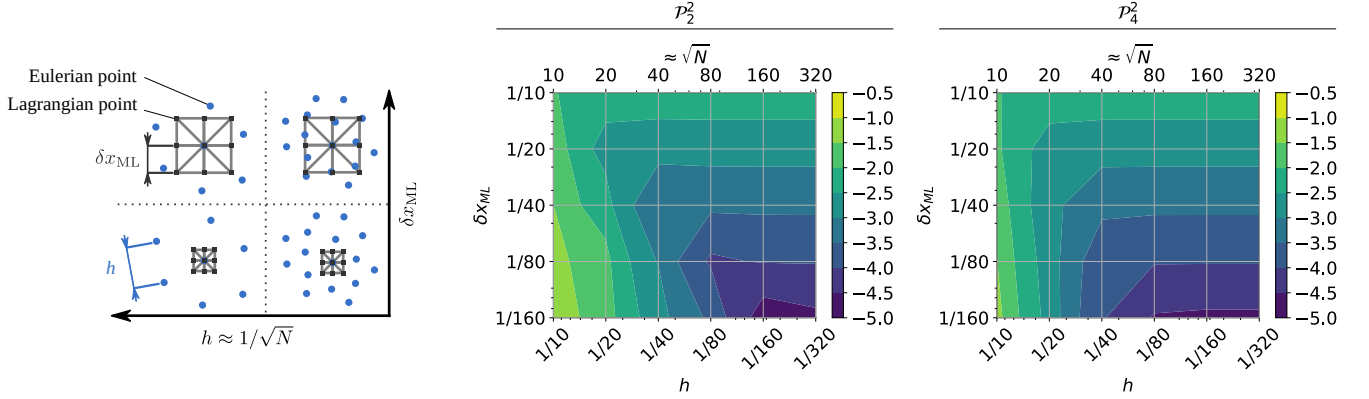


Figure 4. *Left:* in the meshless LBM the streaming distance δx_{ML} (vertical axis) and the interpolation refinement h (horizontal axis) can be altered independently. The choice of these two parameters influences errors introduced by the Boltzmann equation spatial discretization and the interpolation step, respectively. *Middle and right:* \log_{10} of L_2 error norm (Eq. (19)) of the u -component of velocity for the two orders of polynomial subset of the interpolation basis.

For the meshless LBM we use $\delta x_{ML} = 1/10, 1/40, 1/160$ and $h = 1/10, 1/20, 1/40, 1/80, 1/160, 1/320$. For the standard LBM we use $\delta x = 1/10, 1/20, 1/40, 1/80, 1/160$. Such choice of h and δx gives a comparable number of nodes discretizing the domain in each method (the meshless discretizations used have approximately 15% less nodes than the regular ones with $\delta x = h$). We also note that the values of δx_{ML} form a subset of δx values which allows for an easier investigation of the LBM-related errors of the meshless approach. To match time discretizations we set $\delta t = 10^{-3}$ for $\delta x_{ML}, \delta x = 1/10$. To prevent the loss of the second order convergence in $\delta x_{ML}, \delta x$ due to compressibility errors we perform diffusive scaling $\delta t \propto \delta x_{ML}^2, \delta x^2$. For both LBM variants we use $\tau = 0.8$.

The initial condition for the distribution functions was given by the equilibrium populations (Eq. (4)) parameterized with the macroscopic fields from Eq. (18) at $t = 0$ (see Fig. 3).

For the error measure we choose the normalized discrete norm of u -velocity error at time t_{end} (see e.g. ^{33,34}):

$$L_2 = \frac{\sqrt{\sum_{i=1}^N (u_i^{t_{end}} - u_{i,true}^{t_{end}})^2}}{\sqrt{\sum_{i=1}^N (u_{i,true}^{t_{end}})^2}} \quad (19)$$

where the subscript i denotes the value of a variable at node x_i . By transforming the exponential terms in Eq. (18) we choose:

$$t_{end} = \frac{\ln 10}{2\nu k^2} \quad (20)$$

which corresponds to the time, when the vortices have decayed to 10% of their initial magnitude.

The middle and the rightmost plots of Fig. 4 show maps of $\log_{10} L_2$ for the meshless LBM solution in the space of the discretization parameters $\delta x_{ML}, \sqrt{N}$ and h . Each subplot concerns different order of the polynomial part of the interpolation basis. The vertical and bottom horizontal axes are aligned in the same manner as in the leftmost plot, and both maps share the same color scale. It is observed that increasing the order of the polynomial basis results in a decrease in the errors, which is most pronounced in the coarse \sqrt{N} region. For a sufficiently small δx_{ML} there is clear error convergence with h refinement for both polynomial augmentations. However, for larger values of δx_{ML} , error convergence occurs only up to a certain point and then stops. A similar error behavior occurs for smaller values of \sqrt{N} and refinement of δx_{ML} . For the most refined δx_{ML} and largest h even a divergence of the errors is observed, especially for \mathcal{P}_2^2 . Tests performed with orders of the polynomial augmentation below 2 did not yield satisfactory results in the concerned range of δx_{ML} and \sqrt{N} values and thus will be excluded from further discussion.

Fig. 5 shows the same data compared with the error of the standard LBM (black symbols and a solid line). Each column corresponds to a different order of polynomial augmentation and each row concerns a separate $\delta_{x_{ML}}$ value. Here we use \sqrt{N} as the discretization refinement parameter for both methods - compare with the top horizontal axes in Fig. 4. We begin by analyzing $\delta_{x_{ML}} = 1/160$ results (bottom row). For \mathcal{P}_4^2 (right column) the cessation of meshless convergence is observed as early as for $\sqrt{N} \approx 80$. The meshless error reaches then the value of the standard LBM error with $\sqrt{N} = 160$. This discretization refinement in the standard LBM gives the streaming distance $\delta x = 1/160$ which is equal to the used meshless streaming distance $\delta_{x_{ML}} = 1/160$. From this point, continuing the refinement of \sqrt{N} gives no further convergence of the meshless error. In addition, for \mathcal{P}_4^2 the meshless LBM achieves lower errors than the standard LBM for the same number of nodes (green symbols lying below the black curve) for $\sqrt{N} \approx 1/40$ and $1/80$. For \mathcal{P}_2^2 (left column), the meshless LBM error for $\delta_{x_{ML}} = 1/160$ reaches the mentioned LBM error only at $\sqrt{N} \approx 1/320$. However, it surpasses this value at $\sqrt{N} \approx 1/160$ (a green symbol lying lower than the bottommost black dot). This may be explained by the fact that interpolation and LBM-related errors of similar magnitudes cancel each other out. The meshless errors for $\delta_{x_{ML}} = 1/40$ (middle row) behave very similarly to those just described, and their lower bound in the case of a sufficiently refined interpolation discretization (large \sqrt{N}) is the standard LBM error at $\sqrt{N} = 40$. In the case of $\delta_{x_{ML}} = 1/10$ (top row), the corresponding standard LBM error is reached already for the second coarsest \sqrt{N} . We also note that in the convergent regime of \sqrt{N} the meshless results exhibit a higher rate of convergence than that of the standard LBM (which is of the 2nd order).

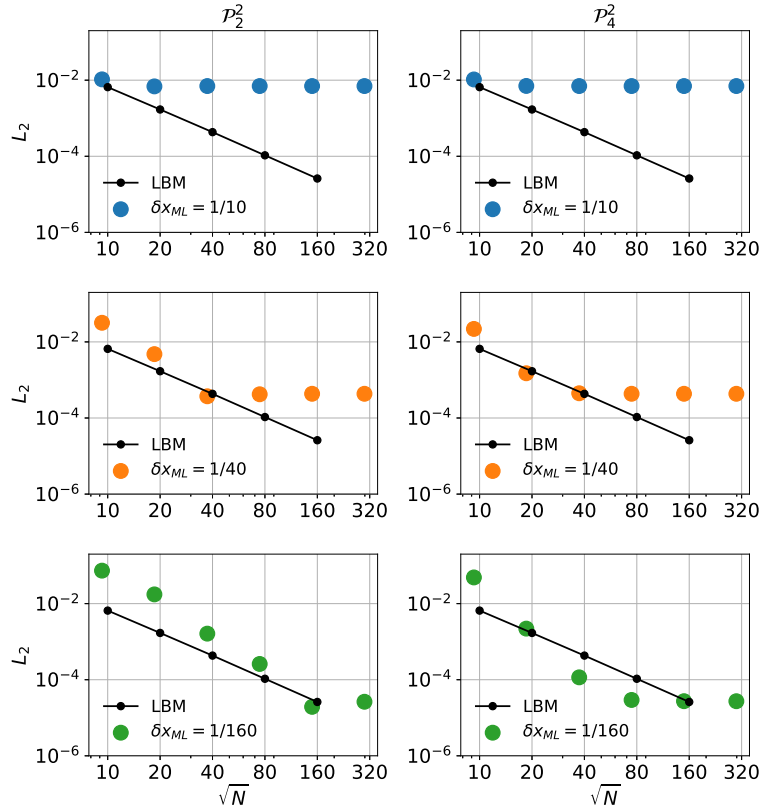


Figure 5. The convergence of L_2 error norm (Eq. (19)) of the u -component of velocity for the Taylor-Green vortex test. Meshless LBM results (*large symbols*) are compared with standard LBM results (*small symbols*). A black solid line connecting the standard LBM results acts as a guide for the eye. Each column corresponds to a different polynomial subset \mathcal{P}_i^2 of the interpolation basis, each row corresponds to a different meshless LBM streaming distance $\delta_{x_{ML}}$.

Fig. 6 shows \log_{10} of the spatial distributions of the velocity magnitude relative error at time t_{end} :

$$e(x_i) \equiv e_i = \frac{\left| |U_i^{t_{end}}| - |U_{i,true}^{t_{end}}| \right|}{|U_{i,true}^{t_{end}}|}, \quad |U_i| = \sqrt{u_i^2 + v_i^2} \quad (21)$$

for the standard LBM and the meshless LBM obtained with the two polynomial augmentations \mathcal{P}_2^2 and \mathcal{P}_4^2 . The standard

LBM results use discretizations of $\sqrt{N} = 11, 41, 161$ such that the nodes do not coincide with zero-velocity coordinates. For the meshless LBM, each row corresponds to a constant δx_{ML} and each column corresponds to a constant \sqrt{N} . For the meshless LBM, 0.5% of the points with the highest and lowest e_i error values are excluded from the visualization. These are nodes with near-zero true velocity magnitudes. Standard LBM errors exhibit a spatial distribution that is symmetric with respect to a rotation about $\pi/2$ angle around the domain center (0.5;0.5) regardless of \sqrt{N} . It can be explained by the same symmetry of the analytical solution, Eq. (18). Four areas in the shape of 0.5×0.5 squares centered at stagnant velocity points (intersections of the dashed lines in Fig. 6) can be clearly distinguished from the error patterns. Let us now relate this observation to the meshless LBM results, starting from the \mathcal{P}_4^2 case (the middle plot of Fig. 6). The same spatial pattern of the e_i error distribution is also observed here for the finest Eulerian points density $\sqrt{N} \approx 160$ (the rightmost column). With a decrease in \sqrt{N} this spatial pattern seems to disappear in favor of some other spatial distribution of errors. This occurs at $\sqrt{N} \approx 40$ and $\sqrt{N} \approx 80$ for $\delta x_{ML} = 1/160$. For \mathcal{P}_2^2 the error spatial pattern similar to that of the standard LBM is visible only for the finest \sqrt{N} and the largest δx_{ML} . Regardless of the order of polynomial augmentation, whenever the standard LBM error pattern appears in the meshless solution, the magnitude of the errors is approximately the same as that in the standard LBM with a similar number of nodes \sqrt{N} . A possible explanation for these phenomena is that for relatively high accuracy of the interpolation (high order of \mathcal{P}_i^2 and fine \sqrt{N}) and large δx_{ML} , the LBM-related errors of the meshless solution are much higher than the interpolation errors, thus the LBM-like spatial pattern is visible. On the other hand, for low accuracy of the interpolation and low LBM-related errors (low order of \mathcal{P}_i^2 , coarse \sqrt{N} , and small δx_{ML}) interpolation errors take over LBM-related errors and a pattern characteristic of the former is visible.

To demonstrate the convergence of the discussed method in the presence of a body force and curved boundaries, we investigate a two-dimensional flow inside an annular channel. The channel walls are circles of radii $R_1=1$ and $R_2 = 2$ centered at the origin. The flow is forced with a constant acceleration $g = (0, g)$ in polar coordinates (r, ϕ) . We implement the body force as an additional term in the collision operator, as suggested in³⁵:

$$f_k^{\text{post}} = f_k(t, x) - \frac{1}{\tau} [f_k(t, x) - f_k^{\text{eq}}(t, x)] + \omega_k \frac{e_k \cdot g}{c_s^2}, \quad (22)$$

and use the value of $g = 10^{-6}$. We apply no-slip boundary condition to the stationary walls of the channel. We assume incompressibility of the fluid, zero radial component of velocity vectors in the whole domain, and rotational symmetry of the velocity and pressure field. The analytical solution of the Navier-Stokes equation with these assumptions is:

$$u(r) = -G(r^2 - \alpha r + \frac{\beta}{r}) \quad (23)$$

where

$$G = \frac{g\phi}{3\nu}, \quad \alpha = \frac{R_1^2 + R_1R_2 + R_2^2}{R_1 + R_2}, \quad \beta = \frac{R_1^2R_2^2}{R_1 + R_2},$$

We perform a series of meshless LBM simulations with the streaming distance $\delta x_{ML} = 1/160$ and Eulerian nodes spacing $h = 1/10, 1/20, 1/40, 1/55, 1/80$ and $1/110$. We set the relaxation time to $\tau = 1$. We use a multireflection bounceback suggested by Ginzburg and d'Humières³⁶. In the meshless LBM, we place the boundary nodes exactly on the boundaries, so the multireflection bounceback reduces to assigning post-streaming population of the opposite lattice direction to the unknown populations:

$$f_k(t+1, x) = f_{k'}(t+1, x) = f_{k'}^{\text{post}}(t, x + e_k) \quad (24)$$

The stencil size is $N_L = 15$ and we use second-order polynomial augmentation for the interpolation. The initial condition is equilibrium distributions for zero macroscopic velocity at each node. The simulation was iterated until the relative u -velocity residual at a given timestep fell below 10^{-10} or up to $5 \cdot 10^5$ iterations. The measure of error is L_2 norm (Eq. (19)) of the velocity magnitude.

Fig. 7 shows the convergence of ML-LBM error as a function of \sqrt{N} (square root of the number of Eulerian nodes). Similarly to the Taylor-Green vortex test, the error convergence has an above-second-order rate for coarser grids, and for the finer ones it reaches its lower limit. One may stipulate that this lower limit would be the error of the standard LBM with $\delta x = 1/160$ and third order (based on the convergence slope in Fig. 7) interpolation in the multireflexion bounceback.

4 Discussion

To explain the observations on the relation between the meshless and the standard LBM error in the absence of walls and body force, we take a look at Eq. (2.81) in³⁷ where the standard LBM error is expressed as:

$$E_{LBM} = (E_{\delta x} + E_{\delta t} + E_{Ma}) = \mathcal{O}(\delta x^2). \quad (25)$$

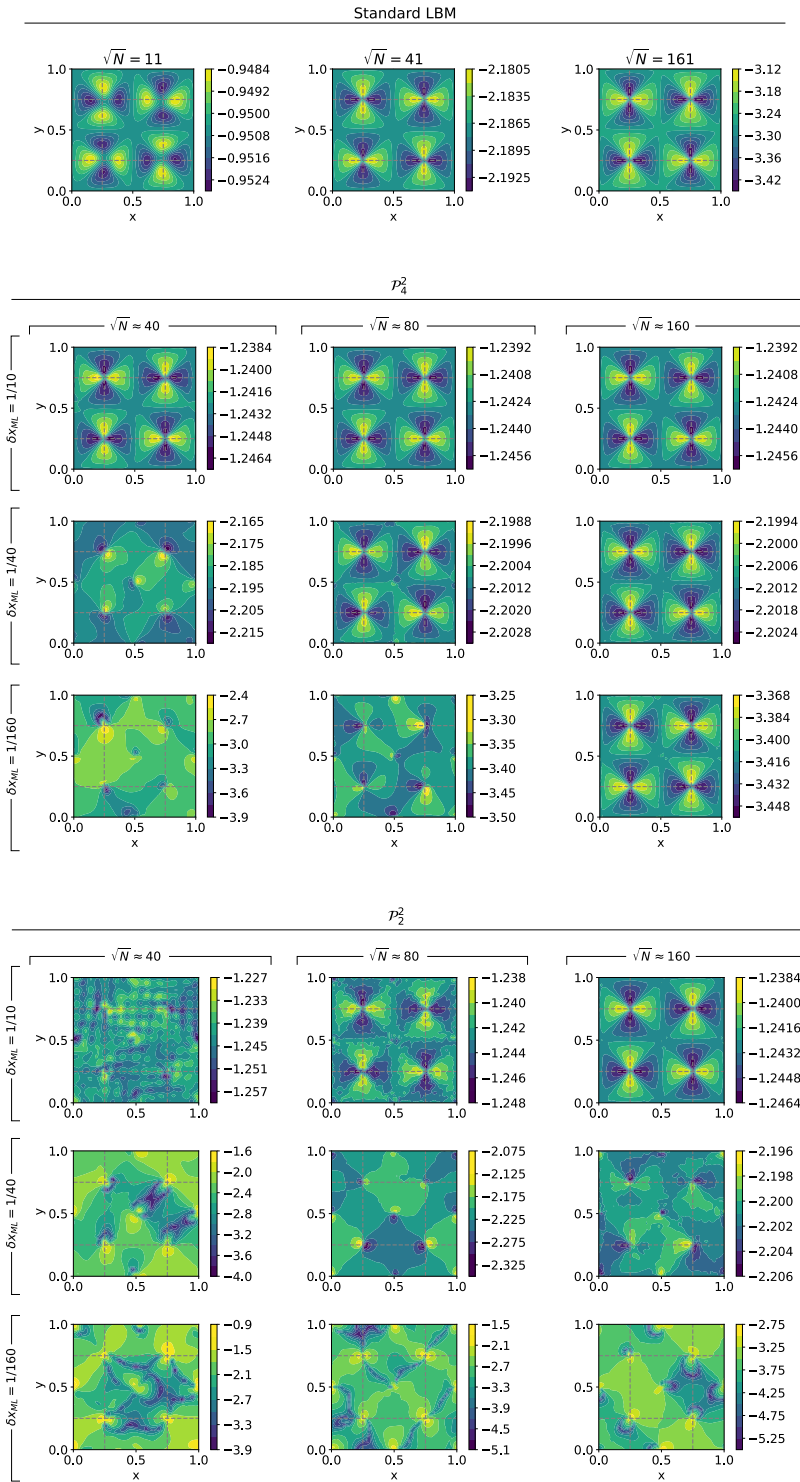


Figure 6. A spatial distribution of relative errors Eq. (21) of the velocity magnitude for the standard LBM (*top*), and the meshless LBM with polynomial augmentation of the second (*middle*) and fourth (*bottom*) order.

Partial errors E_{δ_x} , E_{δ_t} , E_{Ma} are related to space discretization, time discretization, and compressibility, respectively. The last equality above holds when the diffusive scaling of a timestep $\delta t \propto \delta x^2$ is used. Keeping in mind the semi-Lagrangian nature of the streaming step of the discussed meshless LBM one can introduce to Eq. (25) an error term characteristic to semi-Lagrangian

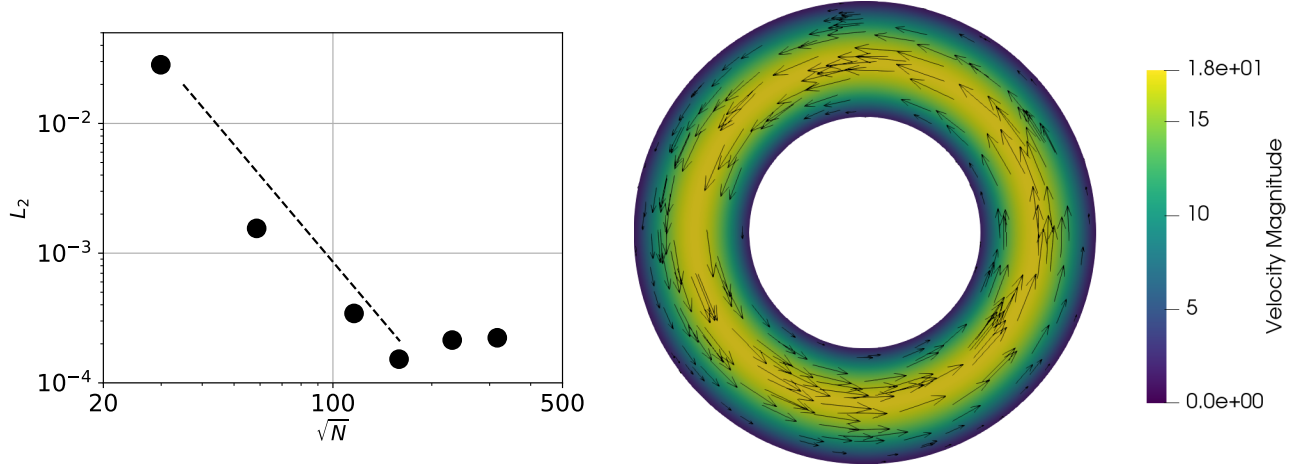


Figure 7. Results of the annular channel flow. *Left:* the convergence of L_2 error norm (Eq. (19)) of the u -component of velocity. Filled dots denote meshless LBM results and the dashed line represents the 3rd order of convergence. *Right:* velocity magnitude field and a few chosen velocity vectors obtained from the meshless LBM simulation.

numerical methods^{38,39}:

$$E_{\text{SL}} = \mathcal{O} \left(\delta x^k + \frac{h^{p+1}}{\delta x} \right) \quad (26)$$

where k depends on the timestepping method used for solving the transport (streaming) step and p is the order of interpolation. In such a way one arrives at the meshless LBM error dependent on the streaming distance δx_{ML} :

$$E_{\text{RBF-LBM}} = \mathcal{O} \left(\delta x_{\text{ML}}^2 + \delta x_{\text{ML}}^k + \frac{h^{p+1}}{\delta x_{\text{ML}}} \right). \quad (27)$$

From the above equation, several phenomena might be predicted. First, decreasing only the semi-Lagrangian part of the error ($\delta x_{\text{ML}}^k + h^{p+1}/\delta x_{\text{ML}}$), which in our case amounted to \sqrt{N} and \mathcal{P}_i^2 refinement, leads to error convergence stagnation, since the LBM-related part ($\sim \delta x_{\text{ML}}^2$), ruled by δx_{ML} and δt , does not fall then and eventually becomes much larger than the semi-Lagrangian streaming errors. Second, decreasing the streaming distance δx_{ML} without accordingly decreasing the Eulerian points distance h or increasing the interpolation order leads to the divergence of the last term in the asymptotic expression in Eq. (27). Meshless LBM errors at a certain δx_{ML} being lower than standard LBM errors with the same $\delta x = \delta x_{\text{ML}}$ may be explained by cancellations of errors introduced by the semi-Lagrangian and LBM terms in Eq. (27). This, however, is visible only when semi-Lagrangian and LBM errors are of similar orders of magnitude. Finally, the meshless LBM can be expected to give lower errors than the standard LBM with the same number of nodes \sqrt{N} only when the order of interpolation $p+1$ is higher than 2 and with sufficiently small δx_{ML} .

The detailed analysis of the error in the case when walls and a body force are present is beyond the scope of this work. Nevertheless, the presented results of the annular channel flow support the previous findings that the discussed meshless LBM variant is convergent in this case as well. The fact that the error convergence stops for some Eulerian discretization refinement suggests that the meshless LBM error relation from Eq. (27) holds also in the presence of walls and body force. The exact value of the lower bound of the meshless LBM error should here depend not only on the standard LBM discretization δx , but also on the implementation of the body force and the no-slip boundaries. According to Guo and others⁴⁰ the forcing scheme used in the present study gives error in Navier-Stokes solution proportional to $\partial g/\partial t$, $\nabla \cdot g$ and $\nabla \cdot gu$. Since for the body force used in our study and for the resulting velocity field (Eq. (23)) the three terms are zero, we find it reasonable to assume that the contribution of the forcing scheme to the error of the macroscopic solution is negligible. Concerning the used bounceback scheme it is not trivial to assess the impact of the implemented multireflection method on the solution error. A comparison with the standard LBM solution with the third-order interpolation in the multireflection bounceback can give some hints into this matter. In practice, the implementation itself can be troublesome, since without the use of e.g. scattered nodes approximation methods, the interpolation stencils have to be adjusted to the local wall normal (even when the symmetries of the lattice discretizing the channel were exploited).

In¹⁹ the authors performed a convergence study of off-grid LBM with linear and quadratic interpolation on rectangular grids and noted the need for the interpolation to have at least the second order of convergence for interpolation errors do not outweigh

LBM errors (compare the exponents 2 and $p + 1$ in Eq. (27)). From their results, one can estimate the orders of convergence as approximately equal to 1.6 when the quadratic interpolation is used. In the present study, the order of convergence for sole interpolation was higher than two for both polynomial augmentation sets \mathcal{P}_2^2 , \mathcal{P}_4^2 (see Fig. 8). As mentioned in Section 3 using a lower-order polynomial augmentation resulted in the lack of a regular behavior of errors in the large \sqrt{N} limit. However, a direct comparison of our results and¹⁹ is difficult since there the standard LBM results were used as a reference for calculating the off-grid LBM errors. Similarly, the authors of²⁰ used Lagrange polynomials on quadrilateral and hexahedral finite elements to perform the interpolation step in an off-grid LBM scheme. Our results are compliant with their findings on the above 2nd-order convergence of velocity error.

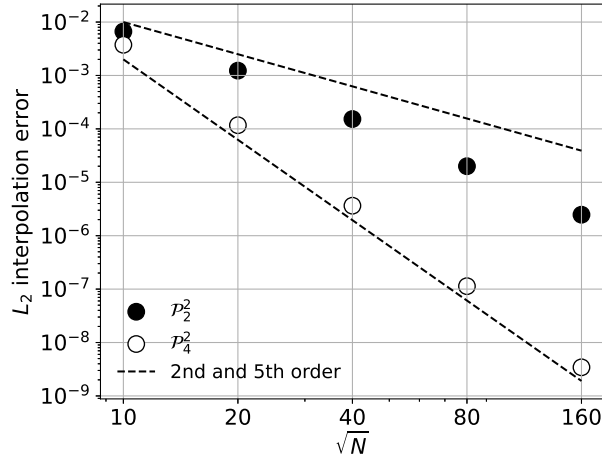


Figure 8. Convergence of the interpolation errors of a function $f(x, y) = 0.01 \sin 2\pi x \cos 2\pi y$ using the same point clouds, stencil size and polynomial subsets of the interpolation basis as in the meshless LBM setups. The interpolation takes place at Lagrangian nodes not coincident with the Eulerian points with the streaming distance $\delta_{x_{ML}} = 1/10$. Dashed lines denote the slopes of the 2nd and the 5th order convergence. The error measure is given by Eq. (19).

The authors of⁴¹ performed a similar error convergence study of an off-grid LBM using the Eulerian approach to solve the streaming step. They report the second-order convergence of L_2 velocity error norm in the Taylor-Green vortex test in the case of using point clouds of Cartesian arrangement (Fig. 3. therein). On the contrary to the present study, those results are obtained with the streaming distance scaled proportionally to the minimal distance between Eulerian points (i.e. $\delta t \propto h/|c_i|_{\max}$ with constant c_i). Along with the lack of any analysis of the order of convergence of the used operator approximation techniques this makes it difficult to tell whether the second-order convergence of the mentioned L_2 norm comes from approximation or LBM-related errors convergence. On the other hand, when the authors of⁴¹ used irregular discretizations (Fig. 4 therein) they obtained above- or below-second-order convergence of the said error norm, depending on the approximation method. This may indicate that the observed convergence is related to the operator approximation error. The convergence results presented in two works of Musavi and Ashrafizaadeh (Fig. 1. in⁴² and Fig. 6. in⁴³) show an error saturation phenomenon similar to the one discussed in the present paper. Our and their results suggest that augmenting the standard LBM with some kind of numerical approximation leads to the saturation of errors regardless of the numerical scheme used to solve the streaming step. We also note that our study concerns a wider range of Eulerian points spacings h than in^{42,43}, and thus we observe a cessation of convergence. We could expect the same in^{42,43} if their study was continued for smaller h . However, one needs to be aware that Pribec⁴¹ and Musavi and Ashrafizaadeh^{42,43} use Eulerian scheme for the streaming step and thus an application of the present conclusions to them should be done with caution.

The further development of the MLBM methods is possible. They can be effectively used in complex LBM models e.g. Shan-Chen single-component multiphase model⁴⁴. In such approaches the interactions between the fluid particles are encoded in the fully local collision operator, which is not affected by any changes made to the streaming step. Moreover, meshless formulation of LBM, with discretization nodes lying exactly on the boundaries, has a potential to simplify the calculation of wall normals, which is known to be problematic in the standard LBM, see e.g. work by Matyka et al.⁴⁵.

5 Conclusions

We show that in the absence of walls and body forces the error of the semi-Lagrangian meshless LBM presented in²⁴ is convergent in the two discretization parameters: \sqrt{N} which controls the interpolation error and δx_{ML} accounting for the LBM-related error (Fig. 4). We show numerically that the lower bound on the meshless LBM error obtained with some value of δx_{ML} is the value of the error of the standard LBM obtained with the discretization giving streaming distance $\delta x = \delta x_{ML}$ (Fig. 5). We observe that increasing the order of interpolation via higher order polynomial augmentation results in a quicker convergence of the meshless LBM error to the said lower bound. In some cases, the meshless LBM can reach significantly lower errors than the standard LBM with the same number of nodes discretizing the domain. We show that the spatial distribution of meshless LBM errors reflects two regimes of the $\sqrt{N}, \delta x_{ML}$ discretization: one dominated by interpolation errors and the other - by LBM-related errors (Fig. 6). Finally, we demonstrate that a similar behavior of the error norm convergence is visible when curved walls and a body force are present.

Acknowledgements

The authors would like to thank the members of Parallel and Distributed Systems Laboratory of Institute *Jožef Stefan* in Ljubljana, Slovenia, for fruitful discussions and insightful remarks on the content of this work.

Funded by National Science Centre, Poland under the OPUS call in the Weave programme 2021/43/I/ST3/00228. This research was funded in whole or in part by National Science Centre (2021/43/I/ST3/00228). For the purpose of Open Access, the author has applied a CC-BY public copyright licence to any Author Accepted Manuscript (AAM) version arising from this submission.

A Meshless LBM algorithm

Algorithm 1 Semi-Lagrangian meshless LBM algorithm (in the absence of walls and body force)

```
1: Data: Set of Eulerian nodes, simulation parameters;
2: for all Eulerian points  $x_i$  do
3:   Initialize the macroscopic variables  $\rho_i$ ,  $u_i$  and  $v_i$  (Eq. (18));
4:   Find stencil members  $x_i^L$ ;
5:   for each lattice velocity  $c_k$  do
6:     Initialize the  $k$ -th distribution function with the equilibrium distribution  $f_k^{\text{eq}}$  parameterized with the initial macroscopic variables (Eq. (4));
7:     Determine the position of the  $k$ -th Lagrangian node  $x_i + \delta t c_k$ ;
8:     Find the closest Eulerian neighbor of the  $k$ -th Lagrangian node;
9:     Calculate shape vector  $w_L(x_i + \delta t c_k)$  for the  $k$ -th Lagrangian node (Eq. (16));
10:   end for
11: end for
12: for the prescribed number of timesteps do
13:   procedure COLLIDE
14:     for all Eulerian points  $x_i$  do
15:       for each lattice velocity  $c_k$  do
16:         Calculate the value of the equilibrium distribution  $f_k^{\text{eq}}$  (Eq. (4));
17:         Calculate the value of the post collision distribution  $f_k^{\text{post}}$  (Eq. (3));
18:       end for
19:     end for
20:   end procedure
21:   procedure STREAM
22:     for all Eulerian points  $x_i$  do
23:       for each Lagrangian point  $x_i + \delta t c_k$  do
24:         Interpolate  $f_k^{\text{post}}$  to  $x_i + \delta t c_k$  (Eq. (16));
25:         Overwrite  $f_{k'}(x_i)$  (the  $k'$ -th distribution at  $x_i$ ) with the interpolated  $f_{k'}^{\text{post}}(x_i + \delta t c_k)$  (Eq. (1));
26:       end for
27:       Update the values of the macroscopic variables (Eq. (6));
28:     end for
29:   end procedure
30: end for
```

References

1. Andrade, J. S., Costa, U. M., Makse, H. A. & Stanley, H. E. Role of Inertia on Fluid Flow through Disordered Porous Media. *Phys. A: Stat. Mech. its Appl.* **266**, 420–424, DOI: [10.1016/S0378-4371\(98\)00624-4](https://doi.org/10.1016/S0378-4371(98)00624-4) (1999).
2. Jin, B. J., Smith, A. J. & Verkman, A. S. Spatial Model of Convective Solute Transport in Brain Extracellular Space Does Not Support a "Glymphatic" Mechanism. *J. Gen. Physiol.* **148**, 489–501, DOI: [10.1085/jgp.201611684](https://doi.org/10.1085/jgp.201611684) (2016).
3. Fu, C., Uddin, M. & Robinson, A. C. Turbulence Modeling Effects on the CFD Predictions of Flow over a NASCAR Gen 6 Racecar. *J. Wind. Eng. Ind. Aerodyn.* **176**, 98–111, DOI: [10.1016/j.jweia.2018.03.016](https://doi.org/10.1016/j.jweia.2018.03.016) (2018).
4. Jasak, H., Vukčević, V., Gatin, I. & Lalović, I. CFD Validation and Grid Sensitivity Studies of Full Scale Ship Self Propulsion. *Int. J. Nav. Archit. Ocean. Eng.* **11**, 33–43, DOI: [10.1016/j.ijnaoe.2017.12.004](https://doi.org/10.1016/j.ijnaoe.2017.12.004) (2019).
5. Baker, T. J. Mesh Generation: Art or Science? *Prog. Aerosp. Sci.* **41**, 29–63, DOI: [10.1016/j.paerosci.2005.02.002](https://doi.org/10.1016/j.paerosci.2005.02.002) (2005).
6. Liu, G. R. & Gu, Y. T. *An Introduction to Meshfree Methods and Their Programming* (Springer-Verlag, Berlin/Heidelberg, 2005).
7. Bayona, V., Flyer, N., Lucas, G. M. & Baumgaertner, A. J. A 3-D RBF-FD Solver for Modeling the Atmospheric Global Electric Circuit with Topography (GEC-RBFFD v1.0). *Geosci. Model. Dev.* **8**, 3007–3020, DOI: [10.5194/gmd-8-3007-2015](https://doi.org/10.5194/gmd-8-3007-2015) (2015).
8. Slak, J. & Kosec, G. Adaptive Radial Basis Function–Generated Finite Differences Method for Contact Problems. *Int. J. for Numer. Methods Eng.* **119**, 661–686, DOI: [10.1002/nme.6067](https://doi.org/10.1002/nme.6067) (2019).
9. Fornberg, B. & Flyer, N. Solving PDEs with Radial Basis Functions. *Acta Numer.* **24**, 215–258, DOI: [10.1017/s0962492914000130](https://doi.org/10.1017/s0962492914000130) (2015).
10. Succi, S. *The Lattice Boltzmann Equation: For Complex States of Flowing Matter* (Oxford University Press, 2018).
11. Matyka, M. & Dzikowski, M. Memory-Efficient Lattice Boltzmann Method for Low Reynolds Number Flows. *Comput. Phys. Commun.* **267**, 108044, DOI: [10.1016/j.cpc.2021.108044](https://doi.org/10.1016/j.cpc.2021.108044) (2021).
12. Koponen, A., Kataja, M. & Timonen, J. Permeability and Effective Porosity of Porous Media. *Phys. Rev. E - Stat. Physics, Plasmas, Fluids, Relat. Interdiscip. Top.* **56**, 3319–3325, DOI: [10.1103/PhysRevE.56.3319](https://doi.org/10.1103/PhysRevE.56.3319) (1997).
13. Paradis, H., Grigoropoulos, C. & Sunden, B. Lattice Boltzmann Modeling for Analysis of Water-Splitting Over Nanorods With Emphasis on Reactive Mass Transport. In *ASME 2013 11th International Conference on Nanochannels, Microchannels and Minichannels, ICNMM 2013*, DOI: [10.1115/ICNMM2013-73098](https://doi.org/10.1115/ICNMM2013-73098) (2013).
14. Gu, Q., Liu, H. & Wu, L. Preferential imbibition in a dual-permeability pore network. *J. Fluid Mech.* **915**, A138, DOI: [10.1017/jfm.2021.174](https://doi.org/10.1017/jfm.2021.174) (2021).
15. Falcucci, G., Jannelli, E., Ubertini, S. & Succi, S. Direct numerical evidence of stress-induced cavitation. *J. Fluid Mech.* **728**, 362–375, DOI: [10.1017/jfm.2013.271](https://doi.org/10.1017/jfm.2013.271) (2013).
16. Coelho, R. C. & Doria, M. M. Lattice Boltzmann Method for Semiclassical Fluids. *Comput. Fluids* **165**, 144–159, DOI: [10.1016/j.compfluid.2018.01.019](https://doi.org/10.1016/j.compfluid.2018.01.019) (2018).
17. Mendoza, M., Boghosian, B. M., Herrmann, H. J. & Succi, S. Fast Lattice Boltzmann Solver for Relativistic Hydrodynamics. *Phys. Rev. Lett.* **105**, DOI: [10.1103/PhysRevLett.105.014502](https://doi.org/10.1103/PhysRevLett.105.014502) (2010).
18. He, X. & Doolen, G. Lattice Boltzmann Method on Curvilinear Coordinates System: Flow around a Circular Cylinder. *J. Comput. Phys.* **134**, 306–315, DOI: [10.1006/jcph.1997.5709](https://doi.org/10.1006/jcph.1997.5709) (1997).
19. He, X., Luo, L. S. & Dembo, M. Some Progress in Lattice Boltzmann Method. Part I. Nonuniform Mesh Grids. *J. Comput. Phys.* **129**, 357–363, DOI: [10.1006/jcph.1996.0255](https://doi.org/10.1006/jcph.1996.0255) (1996).
20. Krämer, A., Küllmer, K., Reith, D., Joppich, W. & Foysi, H. Semi-Lagrangian off-Lattice Boltzmann Method for Weakly Compressible Flows. *Phys. Rev. E* **95**, 1–12, DOI: [10.1103/PhysRevE.95.023305](https://doi.org/10.1103/PhysRevE.95.023305) (2017).
21. Misztal, M. K. *et al.* Simulating Anomalous Dispersion in Porous Media Using the Unstructured Lattice Boltzmann Method. *Front. Phys.* **3**, 1–9, DOI: [10.3389/fphy.2015.00050](https://doi.org/10.3389/fphy.2015.00050) (2015).
22. Bardow, A., Karlin, I. V. & Gusev, A. A. General Characteristic-Based Algorithm for off-Lattice Boltzmann Simulations. *Europhys. Lett.* **75**, 434–440, DOI: [10.1209/epl/i2006-10138-1](https://doi.org/10.1209/epl/i2006-10138-1) (2006).
23. Lee, T. & Lin, C. L. An Eulerian Description of the Streaming Process in the Lattice Boltzmann Equation. *J. Comput. Phys.* **185**, 445–471, DOI: [10.1016/S0021-9991\(02\)00065-7](https://doi.org/10.1016/S0021-9991(02)00065-7) (2003).

24. Lin, X., Wu, J. & Zhang, T. A Mesh-Free Radial Basis Function– Based Semi-Lagrangian Lattice Boltzmann Method for Incompressible Flows. *Int. J. for Numer. Methods Fluids* **91**, 198–211, DOI: [10.1002/fld.4749](https://doi.org/10.1002/fld.4749) (2019).
25. Slak, J. & Kosec, G. On Generation of Node Distributions for Meshless PDE Discretizations. *SIAM J. on Sci. Comput.* **41**, A3202–A3229, DOI: [10.1137/18M1231456](https://doi.org/10.1137/18M1231456) (2019).
26. Krüger, T. *et al.* *The Lattice Boltzmann Method: Principles and Practice*. Graduate Texts in Physics (Springer International Publishing, Cham, 2017).
27. Bhatnagar, P. L., Gross, E. P. & Krook, M. A Model for Collision Processes in Gases. I. Small Amplitude Processes in Charged and Neutral One-Component Systems. *Phys. Rev.* **94**, 511–525, DOI: [10.1103/PhysRev.94.511](https://doi.org/10.1103/PhysRev.94.511) (1954).
28. Crout, P. D. A Short Method for Evaluating Determinants and Solving Systems of Linear Equations with Real or Complex Coefficients. *Transactions Am. Inst. Electr. Eng.* **60**, 1235–1240 (1941).
29. Banachiewicz, T. Méthode de Résolution Numérique Des Équations Linéaires, Du Calcul Des Déterminants et Des Inverses, et de Réduction Des Formes Quadratique. *Bull. Acad. Pol. Ser. A.* 393–404 (1938).
30. Guennebaud, G., Jacob, B. *et al.* Eigen V3 (2010).
31. Taylor, G. I. & Green, A. E. Mechanism of the Production of Small Eddies from Large Ones. *Proc. Royal Soc. London. Ser. A - Math. Phys. Sci.* **158**, 499–521, DOI: [10.1098/rspa.1937.0036](https://doi.org/10.1098/rspa.1937.0036) (1937).
32. Slak, J. & Kosec, G. Medusa: A C++ Library for Solving PDEs Using Strong Form Mesh-free Methods. *ACM Transactions on Math. Softw.* **47**, DOI: [10.1145/3450966](https://doi.org/10.1145/3450966) (2021).
33. Nair, R. D. & Lauritzen, P. H. A Class of Deformational Flow Test Cases for Linear Transport Problems on the Sphere. *J. Comput. Phys.* **229**, 8868–8887, DOI: [10.1016/j.jcp.2010.08.014](https://doi.org/10.1016/j.jcp.2010.08.014) (2010).
34. Lauritzen, P. H., Skamarock, W. C., Prather, M. J. & Taylor, M. A. A Standard Test Case Suite for Two-Dimensional Linear Transport on the Sphere. *Geosci. Model. Dev.* **5**, 887–901, DOI: [10.5194/gmd-5-887-2012](https://doi.org/10.5194/gmd-5-887-2012) (2012).
35. He, X., Zou, Q., Luo, L.-S. & Dembo, M. Analytic solutions of simple flows and analysis of nonslip boundary conditions for the lattice Boltzmann BGK model. *J. Stat. Phys.* **87**, 115–136, DOI: [10.1007/BF02181482](https://doi.org/10.1007/BF02181482) (1997).
36. Ginzburg, I. & d’Humières, D. Multireflection Boundary Conditions for Lattice Boltzmann Models. *Phys. Rev. E* **68**, 066614, DOI: [10.1103/PhysRevE.68.066614](https://doi.org/10.1103/PhysRevE.68.066614) (2003).
37. Latt, J. *Hydrodynamic Limit of Lattice Boltzmann Equations*. Ph.D. thesis (2007). DOI: [10.13097/archive-ouverte/unige:464](https://doi.org/10.13097/archive-ouverte/unige:464).
38. Liu, L. & Becerra, M. An Efficient Semi-Lagrangian Algorithm for Simulation of Corona Discharges: The Position-State Separation Method. *IEEE Transactions on Plasma Sci.* **44**, 2822–2831, DOI: [10.1109/TPS.2016.2609504](https://doi.org/10.1109/TPS.2016.2609504) (2016).
39. Falcone, M. & Ferretti, R. *Convergence Analysis for a Class of High-Order Semi-Lagrangian Advection Schemes*, vol. 35 (SIAM Journal on Numerical Analysis, 1998).
40. Guo, Z., Zheng, C. & Shi, B. Discrete lattice effects on the forcing term in the lattice Boltzmann method. *Phys. Rev. E* **65**, 046308, DOI: [10.1103/PhysRevE.65.046308](https://doi.org/10.1103/PhysRevE.65.046308) (2002).
41. Pribec, I., Becker, T. & Fattahi, E. A Strong-Form Off-Lattice Boltzmann Method for Irregular Point Clouds. *Symmetry* **13**, 1802, DOI: [10.3390/sym13101802](https://doi.org/10.3390/sym13101802) (2021).
42. Musavi, S. H. & Ashrafizaadeh, M. Meshless Lattice Boltzmann Method for the Simulation of Fluid Flows. *Phys. Rev. E - Stat. Nonlinear, Soft Matter Phys.* **91**, DOI: [10.1103/PhysRevE.91.023310](https://doi.org/10.1103/PhysRevE.91.023310) (2015).
43. Musavi, S. H. & Ashrafizaadeh, M. A mesh-free lattice Boltzmann solver for flows in complex geometries. *Int. J. Heat Fluid Flow* **59**, 10–19, DOI: [10.1016/j.ijheatfluidflow.2016.01.006](https://doi.org/10.1016/j.ijheatfluidflow.2016.01.006) (2016).
44. Shan, X. & Chen, H. Lattice Boltzmann Model for Simulating Flows with Multi Phases and components. *Phys. Rev. E* **47**, 1815–1819 (1993).
45. Matyka, M., Koza, Z. & Miroslaw, Ł. Wall orientation and shear stress in the lattice Boltzmann model. *Comput. & Fluids* **73**, 115–123, DOI: [10.1016/j.compfluid.2012.12.018](https://doi.org/10.1016/j.compfluid.2012.12.018) (2013).